Three-dimensional CFD simulation of a circular OWC with a nonlinear power-takeoff: model validation and a discussion on resonant sloshing inside the pneumatic chamber

Conghao Xu[a], Zhenhua Huang[a,*]

[a]*Department of Ocean and Resources Engineering, School of Ocean and Earth Science and Technology, University of Hawaii at Manoa, Honolulu HI 96822 USA*

Abstract

This study presents a three-dimensional numerical simulation of a circular bottom-sitting OWC device for wave energy extraction. The numerical model is based Reynolds-Averaged Navier-Stokes equations with a modified k-ω turbulence model and a Volume-of-Fluid method to track the air-water surface. The numerical model and setup are validated against a set of wave-flume experimental results. The numerical simulation provides detailed flow-field information, which allows for an analysis of the spatial non-uniformity inside the OWC chamber and the measurement error associated with it. New numerical results show that vortex shedding at the sharp edge of the OWC chamber enhances the spatial non-uniformity inside the OWC chamber through a resonant sloshing mechanism. The enhanced spatial non-uniformity can affect the accuracy of the experimentally-determined quantities such as the extraction efficiency of the OWC chamber and the characteristics of the power take-off device; Suggestions are also provided to improve the accuracy of the experimentally-determined quantities that may be affected by the spatial non-uniformity inside the OWC chamber.

Keywords: oscillating water column; numerical modeling; OpenFOAM®; resonant sloshing; wave energy converter

1. Introduction

There has been a rise of interest and practice in obtaining clean and renewable energy technology as the global warming issue becomes a concern and the resources of fossil fuels are depleting. Ocean wave energy is sustainable, clean and abundant (Falnes, 2007). Compared to other clean energy sources such as solar and wind energy, ocean wave energy has less short-term variation and can serve as an important part of the clean energy puzzle.

*Corresponding author contacts:
Email address: zhenhua@hawaii.edu (Zhenhua Huang)

In order to extract ocean wave energy, various types of devices have been proposed (Falcão, 2010); among these devices, Oscillating-Water-Column (OWC) type of wave energy converters (WECs) are widely tested and investigated, mainly due to its robustness in simplicity of wave energy extraction mechanism, easy maintenance, and potentially high energy capture efficiency. A typical OWC-type WEC consists of a semi-submerged and semi-closed pneumatic chamber (referred to as OWC chamber) and a power take-off (PTO) system; the bottom of the chamber allows the ocean waves to create an oscillation of the water mass inside the chamber, which compresses and expands the air volume above the water surface inside the chamber (Evans, 1978). The fluctuating air pressure in the pneumatic chamber drives a power take-off (PTO) turbine, which extracts the wave energy into electricity through a generator.

Since the first theoretical work studying the energy extraction and hydrodynamic characteristics of an OWC device (Evans, 1978), which treats the air-water interface inside the OWC chamber as a rigid weightless piston for simplicity, a wide range of theoretical and experimental studies have been done to provide better understanding of the hydrodynamic processes involved and to improve the energy extraction efficiency of such devices. For example, Evans (1982) extended the theory of Evans (1978) to account for the spatial non-uniformity inside the OWC chamber, and Sarmento and Falcão (1985) examined the effects of the air compressibility in their theoretical study. More recently, matched eigenfunction expansion methods, which are based on linear wave theory, have been applied to study OWC devices with various geometric configurations (Evans and Porter, 1995; Martins-Rivas and Mei, 2008; Lovas et al., 2010; Deng et al., 2013, 2014; Xu et al., 2016). These theoretical studies provide convenient tools to perform frequency-domain analysis of OWC devices for system optimization at the early stage of the system design process. However, because these theories are based on linear wave theory and potential flow assumption, they are usually not able to address issues related to viscous energy loss (i.e., the energy loss associated with vortex shedding) and generation of higher harmonics that may affect the extraction efficiency of the OWC devices.

Scaled laboratory experiments can provide observations of some physical processes and help improve the system optimization of OWC devices. A number of experimental studies on the hydrodynamics and energy extraction of OWC devices can be found in the literature. Existing experimental studies have focused on providing understanding of the wave energy capture efficiency (Wang et al., 2002; He et al., 2013; Ning et al., 2016; Xu et al., 2016; Fleming and Macfarlane, 2017b; Vyzikas et al., 2017), hydrodynamic characteristics such as vortex shedding, wave scattering and the motion responses of floating OWC devices (Rapaka et al., 2004; He et al., 2013; He and Huang, 2014; Xu et al., 2016; Ning et al., 2016; Fleming and Macfarlane, 2017b). Prototype OWC devices have also been put to test over the last few decades (Goda et al., 1991; Boake et al., 2002; Torre-Enciso et al., 2009). Prototype operations have shown that the major challenges in putting OWC devices into the commercial application include the high unit cost of generated electricity and structure survivability under extreme events (Thorpe, 1999; Medina-Lopez et al., 2015).

It has been widely acknowledged that spatial non-uniformity inside the OWC chamber plays a role in the measurement of OWC wave energy capture efficiency. Many small-scale laboratory tests studied two-dimensional OWC chambers (He and Huang, 2014; Bingham et al., 2015; Ning et al., 2016) and used one wave gauge (Wang et al., 2002; Simonetti et al., 2015; Xu et al., 2016) to measure the waves inside the OWC chambers they studied. The use of one wave gauge makes it difficult to accurately determine the mean motion of the air-water surface inside the OWC chamber. He and Huang (2017) proposed a method to reconstruct the water surface inside a rectangular shaped OWC by using two wave gauges, which allows an accurate determination of the water surface inside the OWC chamber. For three-dimensional OWC chamber geometries, however, the use of one or two wave gauges cannot provide enough information to reconstruct the water surface inside the OWC chamber; as a result, the spatial non-uniformity in the water surface may affect the accuracy of the measured capture efficiency. Bingham et al. (2015) used two wave gauges inside the OWC chamber and examined the spatial non-uniformity including sloshing inside the chamber by comparing the measurements of the two wave gauges and visually inspecting the water surface during the experiment. Some experimental studies have also revealed the spatial non-uniformity inside the OWC chamber via CCD camera recordings (Ning et al., 2016) or PIV techniques (Fleming and Macfarlane, 2017b). Vyzikas et al. (2017) placed three wave probes in the width direction of the chamber to examine the lateral sloshing effect inside a rectangular OWC chanber. However, systematic discussion on the spatial non-uniformity and its effect on the measured capture efficiency in both two-dimensional (2D) and three-dimensional (3D) chamber geometries remains rare.

Xu et al. (2016) proposed to use the results provided by a linear frequency-domain solver to reduce the effects of the spatial non-uniformity on the calculation of the energy capture efficiency and the determination of the PTO characteristics. As shown in Xu et al. (2016), the spatial non-uniformity is more significant for shorter waves. However, the generation of higher harmonic waves and their effects cannot be considered in Xu et al. (2016)'s method because of the linear theory used in the analysis. In actual laboratory conditions, short wave components exist in nonlinear incident waves and may also be generated by the higher harmonic components in the fluctuating air pressure due to a nonlinear PTO, nonlinear wave-wave interaction and the vortices shed from the edges of the OWC chamber. These higher harmonic waves may resonate with the OWC chamber, resulting in resonant sloshing mode inside the OWC chamber. These effects of higher harmonics and viscosity that cannot be addressed by frequency-domain solvers can be easily addressed by computational-fluid-dynamics (CFD) simulations. CFD simulations of wave interaction with an OWC device can provide important information about the flow field and the spatial distribution of the water surface inside the OWC chamber, which is otherwise very difficult to obtain in wave-flume tests.

With the development of CFD methods and computing technology, an increasing number of numerical simulations of wave interaction with OWC devices can be found

in the literature. Liu et al. (2008) used a 2D CFD model to study the oscillation amplitude of the water surface inside the OWC chamber and the effect of PTO mechanism on the water column oscillation. Two types of time-domain numerical models have been applied to study the wave power extraction efficiency and the hydrodynamic process of OWC devices in waves: one is based on non-linear potential flow theory(Koo and Kim, 2010; Ning et al., 2015), and the other is based on computational fluid dynamics (CFD), which involves solving the Navier-Stokes equations. Time-domain potential solvers have the advantage of high computational efficiency and are fairly accurate for some problems, but viscous effects cannot be modeled explicitly. Even though non-linear potential solvers such as Higher Order Boundary Element Methods (HOBEM) can be modified to include a parametric consideration of viscous loss (Wang et al., 2018), a detailed and comprehensive modeling of viscous effects can only be provided by CFD models. Zhang et al. (2012) performed CFD simulations based on two-phase level set and immersed boundary method to study the hydrodynamic performance of a 2D OWC device. Teixeira et al. (2013) used a numerical solver based on Navier-Stokes equations and an aerodynamic model in their investigation of optimization of OWC devices. The open source CFD library OpenFOAM® has been used to study bottom-fixed 2D OWC devices (Iturrioz et al., 2015; Simonetti et al., 2015), where the turbulence was handled through either $k-\omega$ SST model or large-eddy-simulation (LES) and the air-water surface was tracked using the Volume-of-Fluid (VOF) method. Comparisons with experimental data have shown that the OpenFOAM®-based simulations can reproduce the experiments well in terms of the chamber pressure and free surface elevations measured at single points, suggesting the potential of using OpenFOAM®-based simulations to further study 3D OWC devices. More recently, Elhanafi et al. (2016) and Elhanafi et al. (2017a) used StarCCM®, which is a CFD software package based on Reynolds Averaged Navier-Stokes Equations (RANS) and VOF method, to study various hydrodynamic and energy conversion aspects of two types of 2D OWC devices. López et al. (2016) proposed to use an RANS-VOF method in a numerical study aimed at finding optimum PTO damping under a given local wave climate. Elhanafi et al. (2017b) studied numerically the impact of air compressibility at different model scaling using compressible and incompressible RANS-VOF methods, it was found that for the three-dimensional OWC device studied, ignoring air compressibility at full scale could introduce an error of 12% in the estimation of power extraction efficiency. All these aforementioned CFD simulations have focused on OWC devices with 2D geometries with the exception of Elhanafi et al. (2017b), and the spatial non-uniformity of the water surface (surface sloshing) inside the OWC chamber is not the focus of these studies.

In this study, we present a numerical simulation of a 3D bottom-sitting OWC device and propose a data analysis method to reduce the effects of spatial non-uniformity (surface sloshing) within an OWC chamber in the calculation of the capture efficiency and the characteristics of the PTO in both the experimental studies and numerical simulations. The numerical model used in this study is based on the open source

CFD library OpenFOAM® with a VOF method to track the air-water surface and a $k-\omega$ turbulence closure. The 3D OWC device is a circular OWC-pile device tested experimentally by Xu et al. (2016). The numerical model and the setup of the numerical wave tank are described in Section 2. The validation of the numerical model and a systematic discussion on the spatial non-uniformity (surface sloshing) as well as the effect of such non-uniformity on the analysis of experimental results are discussed in Section 4, together with suggestions for data analysis to reduce the error induced by spatial non-uniformity. Main conclusions are summarized in Section 7.

2. Description of the numerical model

To facilitate further discussion, the coordinate system used in this paper is defined in Fig. 1, where a sketch of the domain and the coordinate system are shown. The x-axis is horizontal with its positive direction pointing from the wave maker to the wave absorbing zone; the y-axis is vertical with its positive direction pointing vertically upward; the z-axis is horizontal with its positive direction pointing laterally out of the paper.

2.1. Governing Equations

The numerical model is based on the open-source computational fluid dynamics library OpenFOAM®. The model employs the 3D incompressible Reynolds Averaged Navier-Stokes equations (RANS) as the governing equations for a water-air mixture. Let s be the saturation of water in a particular volume: $s = 0$ for the air above the air-water surface and $s = 1$ for the water below the air-water surface. The air-water interface is treated as a thin layer of the water-air mixture where $0 < s < 1$. The density ρ and the dynamic viscosity μ of the water-air mixture are calculated by

$$\rho = s\rho_w + (1-s)\rho_a, \tag{1}$$

$$\mu = s\mu_w + (1-s)\mu_a, \tag{2}$$

where the subscripts w and a refer to water and air, respectively. The continuity equation for the water-air mixture is

$$\nabla \cdot \mathbf{u} = 0, \tag{3}$$

where $\mathbf{u}$ is the velocity field of the water-air mixture. The vector form of the momentum equations is

$$\frac{\partial \rho \mathbf{u}}{\partial t} + \nabla \cdot [\rho \mathbf{u}\mathbf{u}^T] = \rho \mathbf{g} - \nabla p + \nabla \cdot [\mu \nabla \mathbf{u} + \rho \mathbf{T}] + \sigma_T \kappa \nabla \alpha, \tag{4}$$

where p is the pressure, $\mathbf{g}$ is the gravitational acceleration, σ_T is the surface tension constant, κ the curvature of the air-water interface, and $\mathbf{T}$ is the specific Reynolds

stress tensor, which needs to be closed by a selected turbulence model (Rusche, 2003; Versteeg and Malalasekera, 2007).

In order to track the water-air interface, we adopt a modified VOF method, which uses the following phase governing equation

$$\frac{\partial s}{\partial t} + \nabla \cdot [s\mathbf{u}] + \nabla \cdot [\mathbf{u}_r s(1-s)] = 0, \tag{5}$$

with $\mathbf{u}_r$ being an interface compression velocity only present in the water-air interface to suppress the diffusive behavior of the interface. For more details of this modified interface compressive VOF scheme, the reader is referred to Rusche (2003).

The following $k-\omega$ turbulence model is used to provide a closure to the specific Reynolds stress tensor $\mathbf{T}$ (Wilcox, 1993):

$$\frac{\partial \rho\omega}{\partial t} + \nabla \cdot [\rho\mathbf{u}\omega] = \alpha p_\omega - \beta\rho\omega^2 + \frac{\sigma_d}{\omega}\rho\nabla k \cdot (\nabla\omega)^T + \nabla \cdot \left[\left(\mu + \sigma_\omega \rho\frac{k}{\omega}\right)\nabla\omega\right], \tag{6}$$

and

$$\frac{\partial \rho k}{\partial t} + \nabla \cdot [\rho\mathbf{u}k] = p_k - \beta^*\rho\omega k + \nabla \cdot \left[\left(\mu + \sigma^*\mu_t\right)\nabla k\right], \tag{7}$$

where k is the turbulent kinetic energy and ω is a characteristic eddy frequency, p_k and p_ω are the production terms of k and ω, respectively. Following Mayer and Madsen (2000) and Jacobsen et al. (2012), the following forms are adopted for p_k and p_ω in order to suppress the abnormal growth of the turbulent viscosity and turbulent kinetic energy across the interface in potential flows,

$$p_k = \mu_t \left(\nabla \times \mathbf{u}\right) \cdot \left(\nabla \times \mathbf{u}\right)^T, p_\omega = \frac{\omega}{k} p_k, \tag{8}$$

Note that the expressions given in Eq. (8) are different from the original forms of turbulence production terms suggested by (Wilcox, 1993, 2008). The expressions given in Eq.(8) state that the production of turbulent kinetic energy is related to the vorticity of the fluid motion, instead of the shear rate of the fluid velocity.

The dynamic turbulent eddy viscosity μ_t is defined as

$$\mu_t = \rho\frac{k}{\tilde{\omega}}, \tag{9}$$

where

$$\tilde{\omega} = \max\left\{\omega, C_{lim}\sqrt{\frac{2\mathbf{S}:\mathbf{S}}{\beta^*}}\right\}, \tag{10}$$

with $\mathbf{S}$ being the strain rate tensor. The specific Reynolds stress tensor can be calculated by:

$$\mathbf{T} = \frac{2}{\rho}\mu_t\mathbf{S} - \frac{2}{3}k\mathbf{I}, \tag{11}$$

where $\mathbf{S}$ is the strain rate tensor expressed by

$$\mathbf{S} = \frac{1}{2}[\nabla \mathbf{u} + (\nabla \mathbf{u}^T)], \tag{12}$$

and $\mathbf{I}$ is the identity tensor.

We use the following suggested values for the coefficients in the $k - \omega$ model (Wilcox, 2008): $\alpha = 13/25$, $\beta = 0.072$, $\beta^* = 0.09$, $\sigma_\omega = 0.5$, $\sigma^* = 3/5$ and $C_{lim} = 7/8$.

The free, open source CFD software OpenFOAM (Weller et al., 1998) was used to solve these equations with appropriate boundary and initial conditions. A finite volume numerical discretization method on unstructured grids was used to discretize the numerical fields. The pressure-implicit-split-operator (PISO, see, e.g., Ferziger and Peric, 2012; Issa, 1986) method was used for the pressure-velocity coupling solution. A mixed Crank-Nicolson method (Ferziger and Peric, 2012) was used for the discretization in the time domain.

2.2. The OWC model

The OWC device in this study is a numerical reproduction of the circular OWC supported by a C-shaped support structure, which has been studied experimentally and theoretically by Xu et al. (2016). The left panel of Fig. 2 shows a sketch of this OWC model, which consists of a circular tube section covered on the top by a plate with an orifice in it as the PTO mechanism. The upper portion of the model is a partially submerged tube, forming an OWC chamber, and the lower portion of the model is a C-shaped support structure. The overall height of the model is $h = 0.4$ m, the height from the bottom to the top of the C-shaped support structure is $D_s = 0.244$ m, the outer diameter of the model is $D = 0.125$ m, and the orifice diameter is $D_o = 0.014$ m. In the wave-flume tests conducted by Xu et al. (2016), the model was made of stainless steel of 3 mm in thickness, which is used here in the numerical simulations.

2.3. Setup of the numerical wave flume

Referring to Fig. 1, a three-dimensional numerical wave flume of 14.00 m $\times$ 0.54 m $\times$ 0.60 m (length $\times$ width $\times$ height) is used to perform all numerical simulations. The numerical wave flume consists of three sections: the first section (from x=0.00 m to 4.00 m) is the wave generating zone; the second section (from x=4.00 m to 10.00 m) is the test zone; the third section (from x=10.00 m to 14.00 m) is the wave absorbing zone.

The boundary conditions of the numerical wave flume are set up to resemble the actual test conditions in the wave flume tests (Xu et al., 2016): (i) wave inlet boundary conditions are used at x=0 m; (ii) wall boundary conditions are used on the bottom, and two lateral boundaries, and at x=14 m; (iii) atmospheric boundary condition is used at the top boundary of the computational domain; (iv) the walls of the OWC model are set to wall boundaries. All wall boundaries are assumed to be

hydraulically smooth because the walls of the wave flume in the experiment are made of glass and the walls of the OWC model are made of stainless steel.

As in the wave-flume tests (Xu et al., 2016), the numerical OWC model is placed at x=7 m and z=0.25 m, and three numerical wave gauges (G_1, G_2 and G_3) are used to measure the surface displacements inside and outside the OWC model. The locations of G_1, G_2 and G_3 are shown in Fig. 1: G_1 is 5 cm away from the outer edge of the model on the up-wave side; G_2 is inside the OWC chamber, and 3.7 cm away from the geometrical axis of the OWC chamber on the down-wave side of the orifice; G_3 is 5 cm away from the outer edge of the OWC model on the down-wave side. The pressure gauge is placed 3.7cm away from the central axis of the orifice on the up-wave side of the orifice. One numerical pressure gauge is used to measure the air pressure inside the pneumatic chamber. The measured air pressure and the surface displacements at these three locations can be used to verify and validate the numerical model.

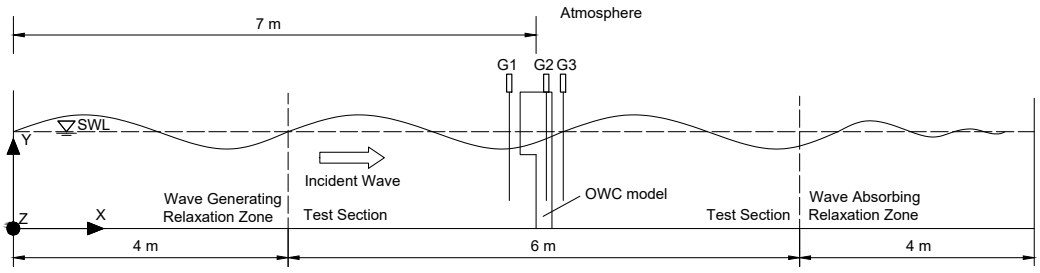

Fig. 1: Sketch of the computational domain. z-coordinate points horizontally out of the paper.

2.4. Wave generation and absorption

In the present study, the wave generation toolbox Waves2Foam (Jacobsen et al., 2012) is implemented to generate monochromatic waves and provide wave-absorbing boundaries. Waves2Foam implements a relaxation-zone for wave generation on top of the VOF-based two-phase flow solver interFOAM (see Chapter 4 of Rusche, 2003). More information about the implementation of Waves2Foam in this study can be found in Appendix B. The method is based on the relaxation-zone concept. On a mesh cell located in the prescribed relaxation zone, physical quantities have prescribed values that are computed using the following expression

$$\phi = \alpha_R \phi_c + (1 - \alpha_R)\phi_t, \tag{13}$$

where ϕ_c is the actual computed value, ϕ_t is the target value, and α_R is the relaxation factor defined by

$$\alpha_R(\chi_R) = 1 - \frac{\exp(\chi_R^{3.5}) - 1}{\exp(1) - 1}, \tag{14}$$

with $\chi_R(= x/L_R)$ being the location relative to the horizontal length of the relaxation zone and L_R the length of the relaxation zone. Thus, it is ensured that at $\chi_R = 0$ (which is the most upstream point), $\alpha_R = 0$ and $\phi = \phi_t$, and at $\chi_R = 1$ (which is the boundary between relaxation zone and non-relaxed zone), $\alpha_R = 1$ and $\phi = \phi_c$. Between these two limits, the value of a physical quantity such as $\mathbf{u}$ or s is a blend of the computed and target values. In this study, the target values are obtained from potential wave theory. Active wave absorption is intrinsically included in the wave-generation relaxation zone.

The relaxation-zone method is also used in the wave absorbing zone to reduce wave reflection. This can be achieved by setting the target value for $\mathbf{u}$ to 0 everywhere in the absorbing zone, and setting the target value for s to the calculated value based on the still water line inside the flume. The length of the relaxation zone was fixed at 4 m in all simulations, which is equivalent to 1.6 to 5.3 wave lengths, depending on the incident wave period. The reflecting coefficient (defined by wave amplitudes) of the relaxation zone for the longest waves considered in this study (T=1.6 s) is 5%, which is comparable in the largest reflection coefficient in the wave flume test. For shorter waves, the reflection coefficient of the relaxation zone is much smaller than 5%.

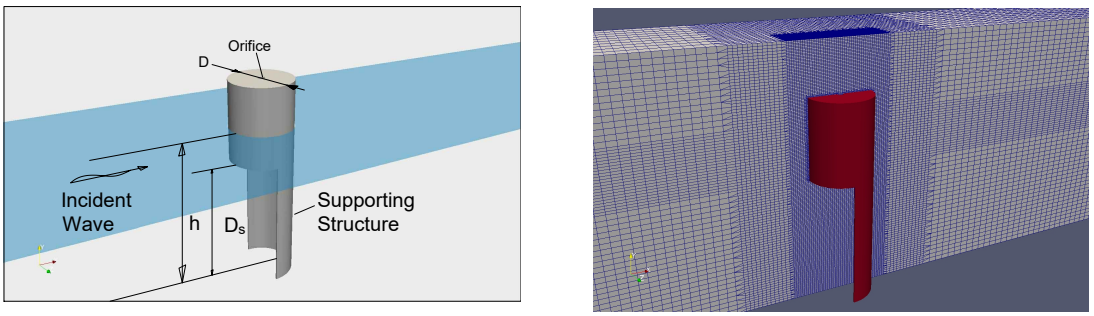

Fig. 2: left: a three-dimensional view of the OWC model as tested in Xu et al. (2016). Right: a view of the mesh configuration in the vicinity of the OWC model.

2.5. Mesh setup

We used an unstructured nested mesh to cover the entire computational domain. The right panel of Fig. 2 shows a slice of the mesh in detail. In order to reduce the computational load, a coarse mesh of resolution 1.64 cm $\times$ 1.00 cm $\times$ 5.00 cm ($\Delta x \times \Delta y \times \Delta z$) was used in the relaxation zones. However, in the test section away from the model, the mesh was refined to a resolution of at least 0.82 cm $\times$ 1.00 cm $\times$ 2.50 cm, which had been confirmed to be fine enough by comparing the simulation results in an empty flume with second-order Stokes wave theory. In order to accurately track the free surface, the mesh within $\pm$5 cm around the still water surface was

further refined to a resolution of 0.82 cm × 0.25 cm × 1.25 cm, representing about 100 horizontal nodes in one wave length and 8 to 20 vertical nodes (covering a single wave length profile of 0.8 s wave period and 2 cm to 5 cm wave height). In the vicinity of the OWC model, an even more refined mesh was used to accurately snap the thin walls of the model, with a characteristic mesh resolution of 0.205 cm × 0.125 cm × 0.159 cm. An OpenFOAM built-in pre-processing mesh tool "snappyHexMesh" was used to deform, re-size and remove mesh cells according to the geometry of the OWC model, resulting in two layers of even finer mesh with a characteristic mesh resolution of 0.1 cm × 0.1 cm × 0.1 cm which closely snaps the surface of the OWC model. The total cell count of the final mesh is about 1.4 million. A the mesh dependence study based on three sets of mesh configurations near the surfaces of the OWC model (a coarser mesh: 1.5 mm x 1.5 mm 1.5 mm; the present mesh:1.0 mm x 1.0 mm x 1.0 mm; and a finer mesh: 0.5 mm x 0.5 mm x 0.5 mm) has confirmed that the quadratic loss coefficients obtained using the present mesh have less than 3% difference from those obtained using the finer mesh. The present mesh was chosen to achieve a balance between computational cost and accuracy.

3. Model verification and validation

This section presents the model verification and validation using the experimental results reported in Xu et al. (2016). These experimental results include the surface displacements measured at three locations inside and around the OWC model, the pressure of the air inside the OWC chamber, and the calculated capture width and the characteristics of the PTO. These results were obtained for 29 test conditions. A typical simulation of about 20 wave periods takes about one week on a high-performance workstation with a total of 20 physical processors (dual Intel Xeon E5-2650 v3) and 128GB of DDR4 memory.

3.1. Physical and numerical test conditions

Table 1 shows a summary of all test conditions used in the model verification and validation. These test conditions have been chosen to test the effects of incident wave period, water depth and wave height on the OWC performance (Xu et al., 2016). The waves generated in the numerical simulations have a maximum difference of 5% in wave height compared to the corresponding waves used in the experiment. The wave heights given in Table 1 are those used in the physical experiment. Experiment A and Experiment B were designed to test effects of wave period and water depth, and Experiment C was designed to test effects of wave height.

3.2. Simulated surface displacement and air pressure inside the OWC chamber

Fig. 3 shows sample comparisons of the simulated and measured surface displacements for two locations outside the OWC chamber: the left panel is for the location G_1 and the right panel is for the location G_3. The left panel of Fig. 4 shows sample

Table 1: A summary of all test conditions

Experiment A: h=0.29 m			Experiment B: h=0.31 m			Experiment C: h=0.31 m		
Case	H (m)	T (s)	Case	H (m)	T (s)	Case	T (s)	H (m)
1a	0.0370	0.7	2a	0.0379	0.7	3a	0.9	0.0157
1b	0.0378	0.8	2b	0.0379	0.8	3b	0.9	0.0261
1c	0.0385	0.9	2c	0.0379	0.9	3c	0.9	0.0460
1d	0.0380	1.0	2d	0.0362	1.0	3d	1.2	0.0170
1e	0.0387	1.1	2e	0.0369	1.1	3e	1.2	0.0271
1f	0.0364	1.2	2f	0.0364	1.2	3f	1.2	0.0472
1g	0.0370	1.3	2g	0.0363	1.3	3g	1.4	0.0170
1h	0.0382	1.4	2h	0.0371	1.4	3h	1.4	0.0272
1i	0.0384	1.5	2i	0.0369	1.5	3i	1.4	0.0474
1j	0.0381	1.6	2j	0.0365	1.6			

comparisons of the simulated and measured surface displacements for the location G_2, which is inside the OWC chamber.

To quantify the comparison between the measurement and the simulation, we use the following normalized root mean square error (NRMSE) as a measure of the closeness between the experiment and the simulation (Ris et al., 1999):

$$\text{NRMSE} = \frac{1}{o_{max} - o_{min}} \sqrt{\frac{1}{N} \sum_{i=1}^{N} (p_i - o_i)^2}, \tag{15}$$

where o_i represents the $i-th$ data point from the experimental observation, o_{max} and o_{min} are the maximum and minimum values occurred in the experimental observation time series used in the analysis, and p_i represents the data point from the model prediction that corresponds to the observation o_i. When NRMSE = 0, a perfect prediction by the simulation is achieved; if NRMSE = 1.0, the root-mean-square error of the simulated time series is comparable to the variation of the observed time series, making the simulation prediction unreliable. In Figures 3 and 4, the values of NRMSE for all comparisons range from 2.18 % to 6.86 %, indicating good agreements between the numerical simulations and the experimental observations.

The right panel of Fig 4 shows comparisons of the simulated and measured variations of the air pressure in the pneumatic chamber. The CFD simulation can capture the air-pressure variation very well, especially the nonlinear features associated with the quadratic nature of the PTO (a small orifice on the top cover of the pneumatic chamber).

The good agreement between the simulated and measured surface displacements at three locations and the air pressure inside the pneumatic chamber indicates that the present CFD model and numerical setup can adequately capture the important physical processes involved in the nonlinear wave interaction with the circular OWC device. Because the detailed flow field inside the OWC chamber can be provided by

the numerical simulation, it is possible to address issues that cannot be addressed by wave-flume experiments, such as surface sloshing and its effects on the extraction efficiency determined using the velocity measured at one point inside the OWC chamber.

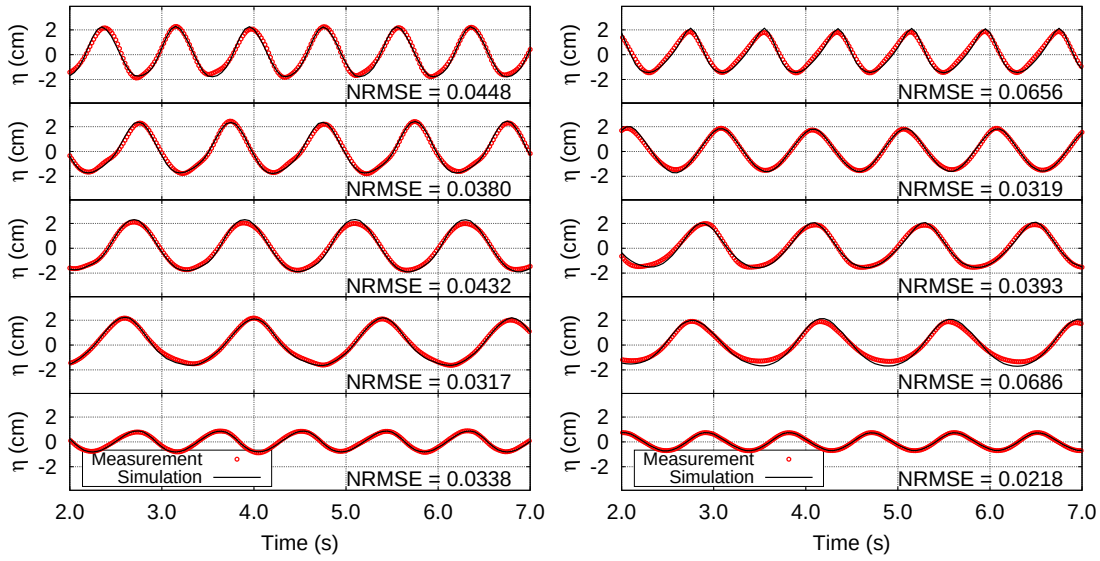

Fig. 3: A comparison of the simulated and measured surface displacements at the location G_1 (left panel) and G_3 (right panel). The five test conditions (from the top to the bottom) are 1b, 1d, 1f, 1h, and 3a. The values next to NRMSE are the normalized root mean square errors defined in Eq. (15).

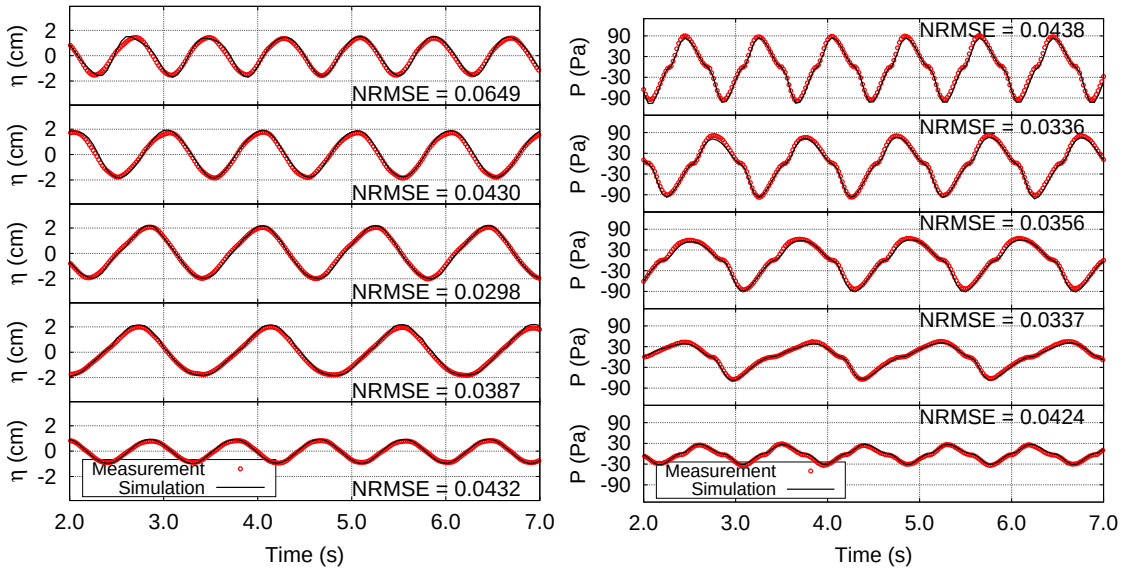

Fig. 4: A comparison between the simulated and measured surface displacements at the location G_2 (left panel) and a comparison between the simulated and measured air pressures inside the pneumatic chamber (right panel). The five test conditions (from top to bottom) are 1b, 1d, 1f, 1h, 3a.

3.3. Extraction efficiency

The extraction efficiency of a wave energy converter is usually measured by the so-called capture width, which is defined as the ratio between the absorbed power and the available wave power per meter of wave crest of the incident waves. For an OWC-type wave energy converter, the wave power extracted by the device, denoted by P_{OWC}, is calculated by

$$P_{OWC} \equiv \frac{1}{NT}\int_{t_0}^{t_0+NT}\left(\iint_S p(t)v(x,z,t)dxdz\right)dt, \tag{16}$$

where S is the cross section of the OWC chamber, $p(t)$ is the air-pressure fluctuation inside the OWC chamber, $v(x,z,t)$ is the local velocity of the oscillation of the water surface inside the OWC chamber, t_0 is an arbitrary time instance, T is the wave period, and N is an integer. The spatial (i.e., cross-sectional) average velocity, $\bar{v}(t)$, is determined by

$$\bar{v}(t) = \frac{1}{A_0}\iint_S v(x,z,t)dxdz \tag{17}$$

with A_0 being the cross-sectional area of the OWC pneumatic chamber. In terms of $\bar{v}(t)$, P_{OWC} can be written as

$$P_{OWC} = \frac{A_0}{NT}\int_{t_0}^{t_0+NT} p(t)\bar{v}(t)dt \tag{18}$$

Therefore the capture width λ can be written as

$$\lambda = \frac{P_{OWC}}{E_I C_g}, \tag{19}$$

where the incident wave energy density E_I and the group velocity C_g are given by

$$E_I = \frac{1}{8}\rho_w g H_I^2, \quad C_g = \frac{L}{T}\left[\frac{1}{2}\left(1+\frac{2kh}{\sinh(2kh)}\right)\right]. \tag{20}$$

In Eqn. (20), h is the local water depth, ρ_w is the density of water, H_I is the incident wave height, L is the wave length, and $k = 2\pi/L$ is the wave number.

The spatial-average velocity $\bar{v}(t)$ is not obtainable in wave-flume experiments (usually a limited number of wave gauges are used to measured the surface motion at selected locations). In most wave-flume tests, the spatial-average velocity $\bar{v}(t)$ is usually approximated by the velocity measured at one single point inside the OWC chamber, say G_2 in our experiment (Xu et al., 2016). We denote the velocity measured at a single point by $\tilde{v}$, and the pneumatic power extraction calculated using $\tilde{v}$, denoted by $\tilde{P}_{OWC}$, is

$$\tilde{P}_{OWC} = \frac{A_0}{NT}\int_{t_0}^{t_0+NT} p(t)\tilde{v}(t)dt, \tag{21}$$

In other words, the capture width measured in the experiment is actually $\tilde{\lambda}$

$$\tilde{\lambda} = \frac{\tilde{P}_{OWC}}{E_I C_g}, \tag{22}$$

The difference between λ and $\tilde{\lambda}$ is affected by the difference between $\bar{v}$ and $\tilde{v}$, which reflects the non-uniformity of the water surface inside the OWC chamber: for a uniform water surface (i.e., a weightless piston), $\bar{v} = \tilde{v}$ and $\lambda = \tilde{\lambda}$. If there is a surface sloshing, we should expect $\bar{v} < \tilde{v}$ and $\tilde{\lambda} > \lambda$.

The capture width is usually normalized by either the wave length (Lovas et al., 2010; Martins-Rivas and Mei, 2008) or a characteristic dimension of the energy converter (Xu et al., 2016). We choose the diameter of the OWC model (D) to normalize the capture width and refer to λ/D as the capture width ratio (CWR) in this study. Fig. 5 shows a comparison of the capture width ratios obtained from the CFD simulation and the experiment for the three sets of the experiments listed in Table 1. It can be seen that the CFD simulation can reproduce the measured capture width ratios ($\tilde{\lambda}/D$) very well, implying that the present CFD simulation can reproduce satisfactorily both the magnitudes and phases of the air-pressure fluctuation and the water-surface oscillation inside the OWC chamber.

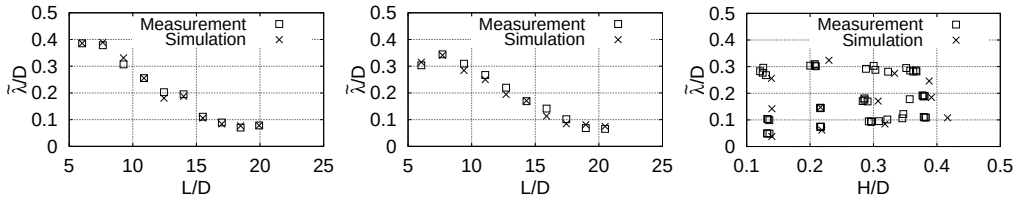

Fig. 5: Comparisons between the simulated and measured values of the capture width ratio ($\tilde{\lambda}/D$) for Experiment A (left), Experiment B (middle) and Experiment C (right): $h/D = 2.32$ (left) and $h/D = 2.48$ (middle).

3.4. Parameterization of the nonlinear PTO

When using potential flow theory to study wave-interaction with an OWC device with a quadratic nonlinear PTO, in frequency domain or time domain, a parametrization of the PTO is needed. In wave-flume tests, the PTO is usually modeled by an orifice, which causes a pressure drop between the pneumatic chamber and the surrounding air outside. For incompressible air, this pressure drop can be modeled by the following equation (Mei et al., 1989; Xu et al., 2016)

$$p(t) = \frac{1}{2} C_f \rho_a \left|\bar{v}(t)\right| \bar{v}(t) + \rho_a L_g \frac{d\bar{v}(t)}{dt}, \tag{23}$$

where $p(t)$ is the relative pressure of the air inside the pneumatic chamber, ρ_a the density of the air, $\bar{v}(t)$ the spatial average velocity of the water-surface oscillation inside the OWC chamber, C_f is a quadratic loss coefficient related to drag effect, and

L_g is an inertial length scale. It has been shown that the inertial effect represented by the last term in Eq. (23) is not important in small-scale wave-flume tests (Xu et al., 2016). Therefore, the nonlinear PTO can be parametrized by the quadratic loss coefficient C_f alone. We remark that the non-uniformity of the water surface inside the OWC chamber can introduce significant error in the value of C_f determined using Eq. (23) and the local velocity measured at a single point inside the OWC chamber.

In the wave-flume experiment of Xu et al. (2016), $p(t)$ was measured by a pressure sensor mounted on the top of the OWC pneumatic chamber, the surface displacement was measured at one location G_2 inside the OWC chamber. Therefore the spatial average velocity $\bar{v}$ is not obtainable from the wave flume experiment, but approximated by $\tilde{v}(t)$, the local velocity measured at the location G_2, which itself needs to be calculated using the surface displacement measured at the location G_2. We use $\tilde{C}_f$ to denote the quadratic loss coefficient determined by using velocity $\tilde{v}$:

$$p(t) = \frac{1}{2}\tilde{C}_f \rho_a \left|\tilde{v}(t)\right| \tilde{v}(t), \tag{24}$$

where the inertial term has been neglected (Xu et al., 2016).

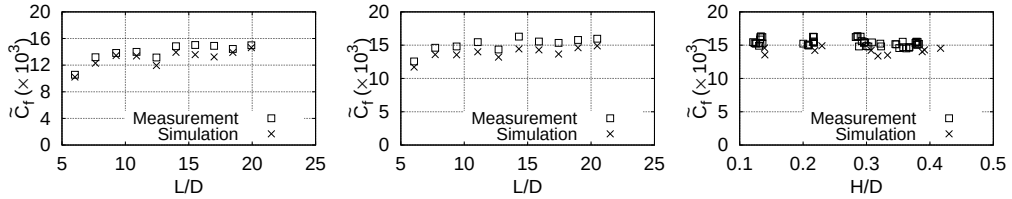

Fig. 6: Comparisons between the simulated and measured values of $\tilde{C}_f$ for Experiment A (left), Experiment B (middle) and Experiment C (right): $h/D = 2.32$ (left) and $h/D = 2.48$ (middle and right).

The measured and simulated values of $\tilde{C}_f$ are shown in Fig. 6. A satisfactory agreement between the simulation and the experiment can be observed for all test cases: the minor difference is due mainly to the minor difference in the local velocity $\tilde{v}$ obtained from the experiment and the simulation.

4. Spatial non-uniformity and resonant sloshing inside the OWC chamber

Because the cross-sectional dimension of a typical OWC device is smaller than the wave length of design waves, the spatial non-uniformity in the water surface inside the OWC chamber is expected to be stronger for shorter waves than for longer waves. Using the CFD simulation results, we are able to obtain detailed flow information, which can help understand factors that affect the spatial non-uniformity and reduce the measurement error in the determination of capture width and the characteristics of the PTO.

4.1. Spatial non-uniformity inside the the OWC chamber

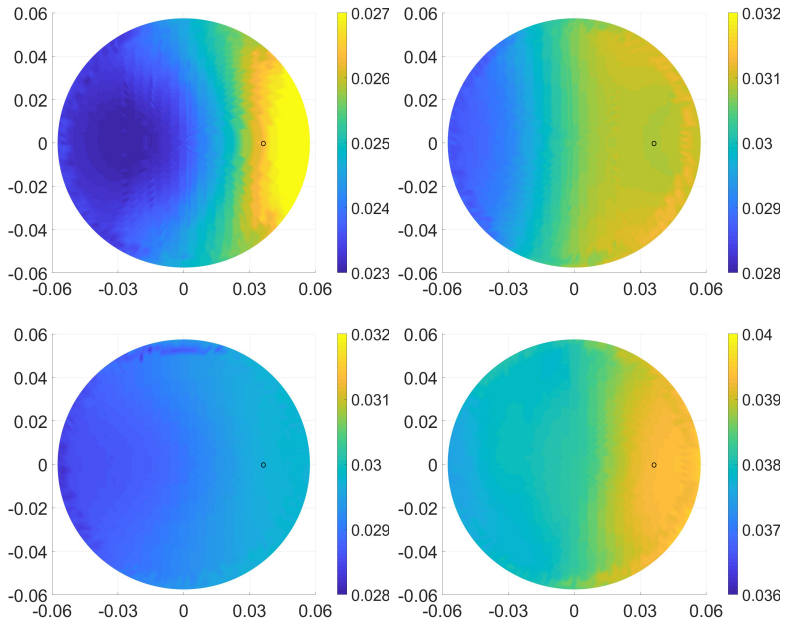

Fig. 7: Distributions of the wave height inside the OWC chamber. From left to right and from top to bottom: Case 1a (t=0.7 s, h=0.29 m); Case 1b (t=0.8 s, h=0.29 m); Case 1e (t=1.1 s, h=0.29 m); Case 2b (t=0.8 s, h=0.31 m). The circle on each plot indicates the location of the wave gauge G_2 in the experiment of Xu et al. (2016)

One way to show the spatial non-uniformity of the water surface inside the OWC chamber is the spatial distribution of the wave height inside the OWC chamber as shown in Fig. 7, where the wave height is the vertical distance between the local maximum and the local minimum of the surface displacement measured within one wave period. Because there exists a partial standing wave pattern in front of the C-shaped support structure, the wave height is larger closer to this reflective boundary. Both the wave period and the draft of the OWC chamber affect the non-uniformity of the water surface inside the OWC chamber: shorter waves generally give a stronger spatial non-uniformity, which is in general agreement with our intuition and the theoretical predictions of Xu et al. (2016). Increasing the draft of the OWC chamber reduces the non-uniformity of the water surface inside the OWC chamber. Because the velocity obtained at a single location is used to represent the spatial-averaged velocity, there is an error introduced to the calculated capture width λ and the quadratic loss coefficient C_f.

4.2. Spectral analysis of the sloshing motion inside the OWC chamber

To further understand the non-uniformity of the water surface inside the OWC chamber, the simulated surface displacement $\eta(x, z, t)$ is decomposed into two com-

ponents: the cross-sectional average and the deviation from this spatial average.

$$\eta(x,z,t) = \bar{\eta}(t) + \eta'(x,z,t), \tag{25}$$

where $\eta'(x,z,t)$ (the sloshing component) is the deviation from the cross-sectional average component $\bar{\eta}(t)$ (the spatial mean component)

$$\bar{\eta}(t) = \frac{1}{A_0}\iint_S \eta(x,z,t)dxdz \tag{26}$$

with S being the cross section of the OWC chamber. By definition,

$$\iint_S \eta'(x,z,t)dxdz = 0 \tag{27}$$

In Eq. (25), $\bar{\eta}(t)$ represents a piston-like oscillation inside the OWC chamber, and $\eta'(x,z,t)$ represents the spatial non-uniformity superimposed on $\bar{\eta}(t)$. We refer to the motion associated with $\bar{\eta}$ as "spatial-average motion" and the motion associated with $\eta'(x,z,t)$ as "sloshing motion" hereinafter.

In a wave-flume experiment, the surface displacement is measured at a very limited number of points. As a result, the spatial-average motion $\bar{\eta}(t)$ is not measurable, so is the sloshing motion $\eta'(x,z,t)$. In their wave-flume experiment, Xu et al. (2016) approximated the spatial-average motion $\bar{\eta}(t)$ by the surface displacement measured at the location G_2 (see Fig. 1). When the surface displacement is measured at a given point, say G_2 in the experiment of Xu et al. (2016), the harmonic components in the spatial-average motion $\bar{\eta}(t)$ and the sloshing motion $\eta'(t)$ can be studied through an harmonic analysis. To understand the relationship between the incident waves and the motion of the air-water surface inside the OWC chamber, we use the simulated data to show the spectral characteristics of the incident waves, the spatial average motion and sloshing motion inside the OWC chamber. We use $\eta'(t)$ to represent $\eta'(x_{G_2}, z_{G_2}, t)$ for simplicity hereinafter.

The incident waves can be expressed as

$$\eta_I = \frac{1}{2}\int_{-\infty}^{\infty} A(f)e^{-2\pi ift}df, \tag{28}$$

and the amplitude spectrum of $\eta_I(t)$ is $|A(f)|$. The displacements for the spatial-average motion and the sloshing motion can be expressed as

$$\bar{\eta} = \frac{1}{2}\int_{-\infty}^{\infty} \bar{B}(f)e^{-2\pi ift}df, \quad \eta'(t) = \frac{1}{2}\int_{-\infty}^{\infty} B'(f)e^{-2\pi ift}df \tag{29}$$

and the amplitude spectra of $\bar{\eta}(t)$ and $\eta'(x,z,t)$ are $|\bar{B}(f)|$ and $|B'(f)|$, respectively. The Matlab built-in Fast Fourier Transfer (FFT) function was used to perform the spectrum analysis in this study. The FFT analysis was performed only on the stable

segment of the signal which consists of several stable waves . The length of the signal was carefully chosen so that energy leaking between frequency bins is minimized.

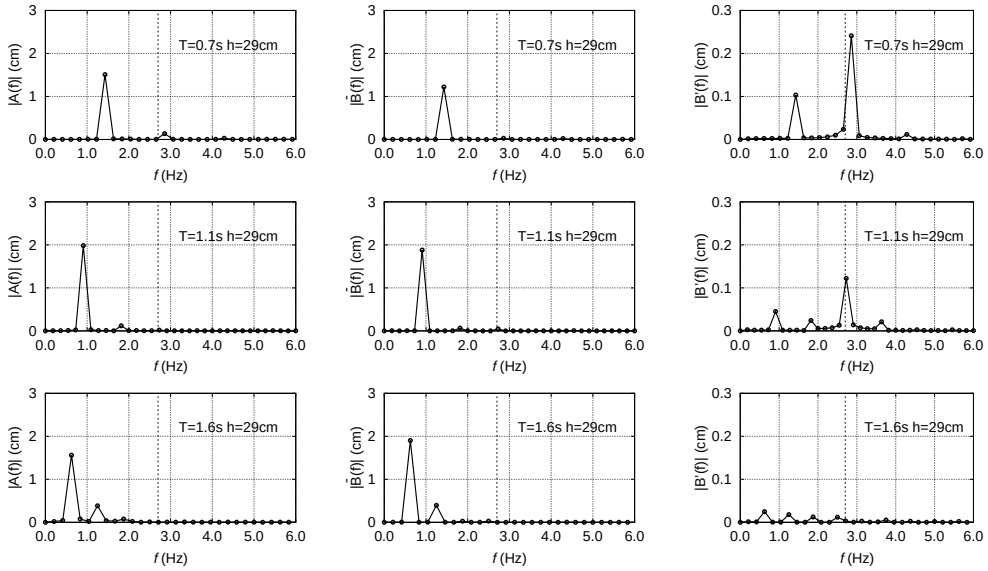

Fig. 8: The simulated amplitude spectra of $\eta_I(t)$, $\bar{\eta}(t)$ and $\eta'(t)$ for three test cases (T=0.7, 1.1 and 1.6 s) in Experiment A.

Fig. 8 shows the simulated amplitude spectra $|A(f)|$, $|\bar{B}(f)|$ and $|B'(f)|$ for three cases (T=0.7, 1.1, and 1.6 s) selected from Experiment A (h=0.29 m). The surface displacement measured at G_1 is due mainly to wave diffraction. It was used to approximate the main features in the incident waves. The displacements for the spatial-average motion and the sloshing motion are obtained using the surface displacement at the location of G_2. The vertical dashed line at f_n=2.717 Hz in Fig. 8 indicates the resonant sloshing frequency of the OWC chamber (see Deng et al., 2013; Xu et al., 2016), which corresponds to a wave length about 1.8 times the diameter of the OWC chamber. Because the higher harmonic locked waves all have the same phase speed as that of the incident fundamental waves (i.e., the second harmonic locked waves have a length that is one half of the length of the first harmonic incident waves, and the third harmonic locked waves have a length that is one third of the length of the first harmonic incident waves), the resonant sloshing motion discovered by Deng et al. (2013) and Xu et al. (2016) is a free standing wave whose phase speed is not locked to that of the incident waves. For all three wave periods, even though the incident waves have weak second harmonic components, the third harmonic components in the incident waves are negligibly small. Among the three wave periods, the incident waves with T=1.6 s have a relatively larger second harmonic component, which is about 25% of the amplitude of the first harmonic component.

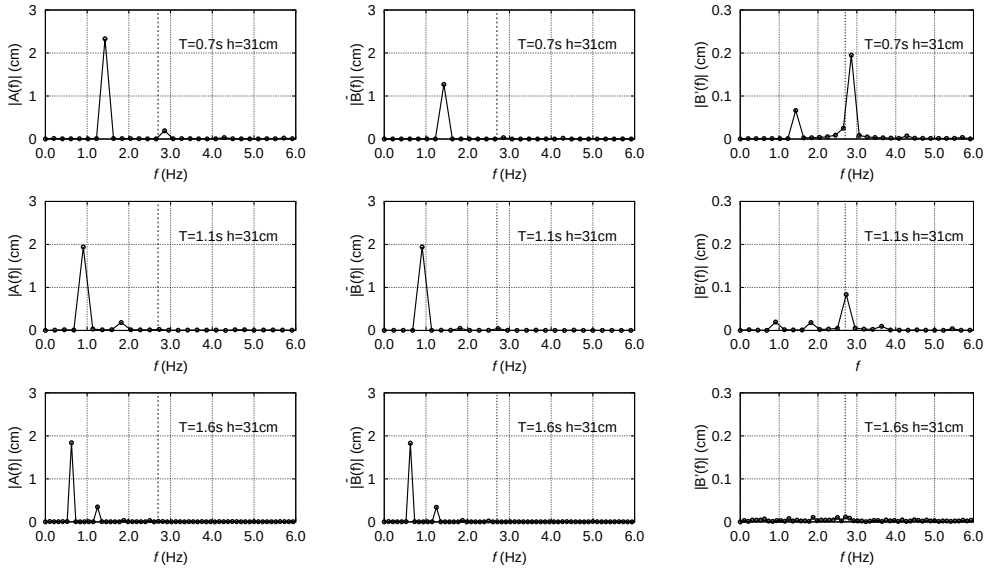

Fig. 9: The simulated amplitude spectra of $\eta_I(t)$, $\bar{\eta}(t)$ and $\eta'(t)$ for three test cases (T=0.7, 1.1 and 1.6 s) in Experiment B.

Refer to the first row in Fig. 8 for T=0.7 s, the amplitude of the first harmonic oscillation in the spatial-average motion is slightly smaller than that in the incident waves. The first harmonic in the sloshing motion also contributes to the non-uniformity of the water surface inside the OWC chamber. The amplitude of the second harmonic in the spatial-average component is negligibly small; however, it is significantly large in the sloshing component, as large as 20% of the amplitude of the first harmonic in the spatial-average component. We remark here that the second harmonic sloshing motion has a frequency close to the OWC's resonant sloshing frequency.

Refer to the second row in Fig. 8 for T =1.1 s, the spatial-average motion is dominated by the first harmonic motion, which has an amplitude similar to that of the incident waves. The sloshing motion is dominated by the third harmonic motion whose frequency is almost identical to that of the OWC's resonant sloshing frequency. The sloshing motion has a first harmonic component similar to that for T=0.7 s, but both the second and fourth harmonic component are small.

Refer to the third row in Fig. 8 for T=1.6 s, in addition to the first harmonic motion, the spatial-average motion has also a noticeable second harmonic oscillation whose amplitude is larger than that of the incident waves. The higher harmonics in the sloshing motion are all weak, which is in agreement with the generally accepted conclusion that the water surface acts like a weightless position for longer waves (Evans, 1982). No resonant sloshing occur for longer waves.

Fig. 9 shows the simulated amplitude spectra $|A(f)|$, $|\bar{B}(f)|$ and $|B'(f)|$ for three cases (T=0.7, 1.1, and 1.6 s) selected from Experiment B (h=0.31 m). For all three wave periods, even though the incident waves have weak second harmonic compo-

nents, the third harmonic components in the incident waves are negligibly small. The vertical dashed line at f_n=2.717 Hz indicates the resonant frequency of the OWC chamber (see Deng et al., 2013; Xu et al., 2016), which corresponds to a wave length about 1.8 times the diameter of the OWC chamber. For a given design of the OWC pile, a deeper water depth means a deeper draft (or submergence) of the OWC chamber. Similar to h=0.29 m, the resonant sloshing occurs at the second harmonic for T=0.7 s, and the resonant sloshing occurs at the third harmonic for T=1.1 s. A comparison of Figs. 8 and 9 shows that slightly increasing the draft can slightly reduce the first harmonic amplitudes in both the spatial-average motion and sloshing motion, but can noticeably reduce the higher harmonic amplitudes in the sloshing motion.

From Figs. 8 and 9, some important conclusions about the sloshing motion inside the OWC chamber can be drawn. For T=0.7 s, resonant sloshing is excited by a second harmonic forcing; for T=1.1 s, the resonant sloshing is excited by a third harmonic forcing. For T=1.6 s, there is no resonant sloshing. The excitation forcing that feeds energy into resonant sloshing cannot be the higher harmonic locked waves for two reasons: (i) the third harmonic locked waves in the incident waves for T=1.1 s have a strength too weak to provide enough energy to excite the resonant sloshing; (ii) the resonant sloshing has a wave length about 1.8 times the OWC diameter, which is much shorter than the lengths of the second and third harmonic locked waves,. Therefore, it is not the second or third harmonic locked waves that provide the excitation forcing through wave-wave nonlinear interaction.

Other possible nonlinear mechanisms that may be responsible for exciting the resonant sloshing inside the OWC chamber are: (i) the air flow through the nonlinear PTO and (ii) vortex shedding. Because the PTO in the experiment was an orifice, which has a quadratic relation with the spatial-average velocity of the water surface inside the OWC chamber, the nonlinear PTO may play a role in exciting the resonant sloshing. Vortex shedding at the lower tip of the OWC front skirt may perturb the flow field inside the OWC chamber and thus may play a role in exciting the resonant sloshing.

4.3. Sloshing motion in the OWC chamber without PTO

The nonlinear PTO described by Eq. (23) can generate higher harmonic components in the fluctuating air pressure $p(t)$. It is interesting to know whether or not the higher harmonic sloshing in the OWC chamber is related to the nonlinear PTO. For this purpose, another set of CFD simulations were performed with the PTO being removed from the top cover so that the OWC chamber is fully open to the surrounding air (i.e., the pressure on the water surface is the constant atmospheric pressure). Figs. 10 and 11 show the simulated amplitude spectra of the incident waves, the spatial-average motion and the sloshing motion for Experiment A and Experiment B, respectively. For a fully-opened OWC, the spatial-average motion is dominated by the first harmonic oscillation but the sloshing motion is dominated by higher harmonics.

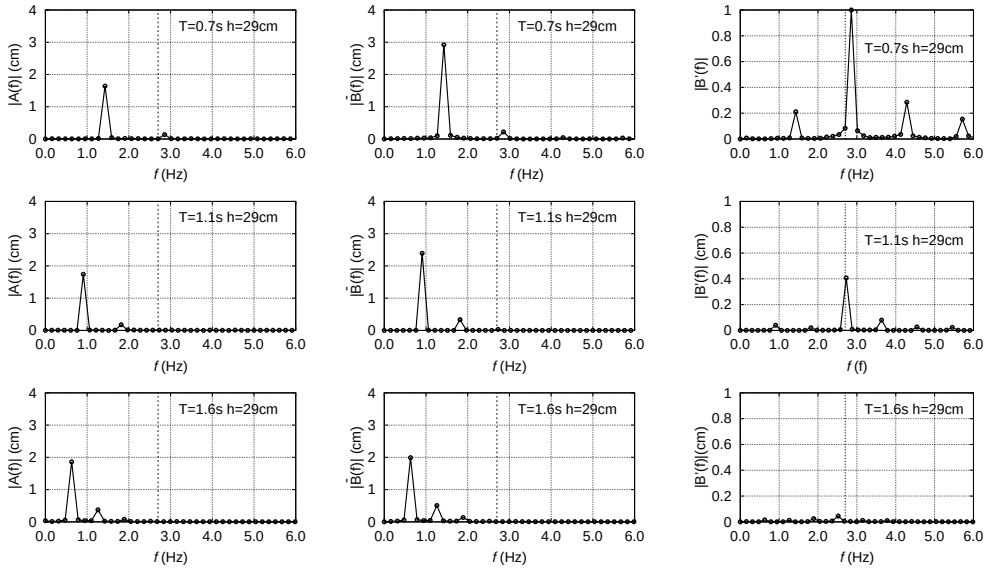

Fig. 10: Plots of the spectral analysis for the simulated η_I, $\bar{\eta}(t)$ and $\eta'(t)$ (taken at the location G_2) for selected test wave conditions with the OWC chamber fully opened to the air. $h = 0.29$ m.

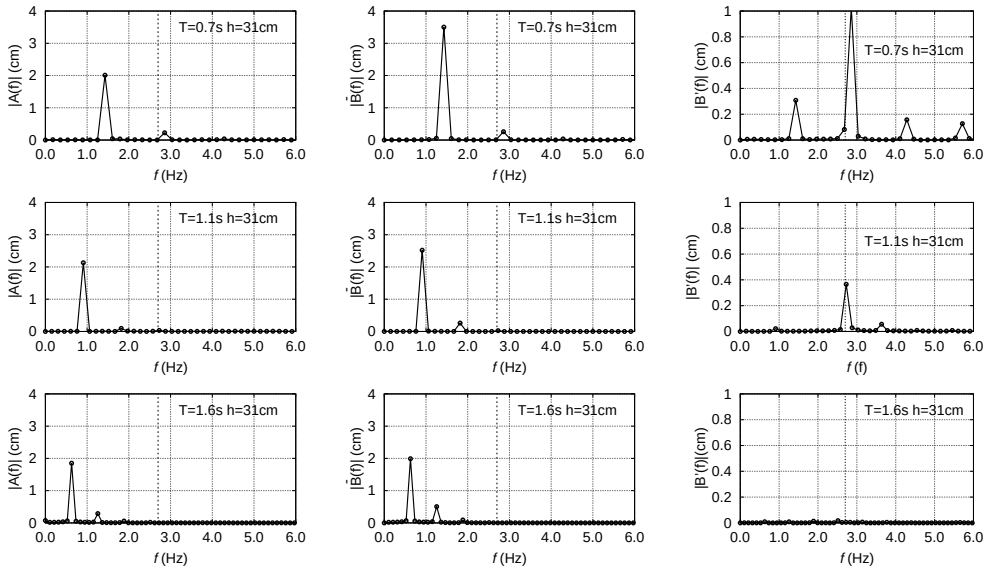

Fig. 11: Plots of the spectral analysis for the simulated η_I, $\bar{\eta}(t)$ and $\eta'(t)$ (taken at the location G_2) for selected test wave conditions with the OWC chamber fully opened to the air. $h = 0.31$ m.

For T=0.7 s, the amplitude of the first harmonic in the spatial-average motion is almost two times that of the corresponding incident waves, and the sloshing motion is dominated by the second harmonic motion whose amplitude can reach about 60% of the amplitude of the first harmonic in the incident waves. The third and fourth harmonic components can also be identified in the sloshing motion. For this case, the frequency of the second harmonic is close to that of the resonant sloshing. Note that

the third and fourth harmonics are negligibly small in the incident waves. Compared to the case with a PTO, the pressure fluctuation inside the OWC chamber suppresses the amplitudes of both the spatial-average motion and the sloshing motion.

For T=1.1 s, the first harmonic amplitude of the spatial-average motion is almost 1.5 times that of the corresponding incident waves, and the sloshing motion is dominated by the third harmonic motion whose amplitude can reach about 20% of the first harmonic amplitude of the incident waves. The fourth harmonic is also noticeable in the sloshing motion. For this case, the frequency of the third harmonic sloshing motion is close to that of the resonant sloshing. Note also that the third and fourth harmonics are negligibly small in the incident waves. Again, compared to the case with a PTO, the pressure fluctuation inside the pneumatic chamber suppresses the amplitudes of both the spatial-average motion and the sloshing motion.

For T=1.6 s, the first harmonic amplitude of the spatial-average motion is almost the same as that of the corresponding incident waves, but the sloshing motion is not present.

It can be concluded that the resonant sloshing motion in the OWC chamber is not excited by the nonlinear PTO. Even though the resonant sloshing is not excited by the air-pressure fluctuation introduced by the nonlinear PTO, but the nonlinear PTO can suppress both the spatial-average motion and the sloshing motion through generation of radiated waves.

4.4. Excitation of resonant sloshing by vortex shedding

If the resonant sloshing motion inside the OWC chamber is not exited by the nonlinear PTO or the higher harmonic wave components in the incoming waves, it may be exited by the vortex shedding at the sharp edges of the OWC pile. Wave-induced vortex shedding is a viscous, nonlinear process. To understand the relation between the vortex shedding and the resonant sloshing, we examine the spectrum of the computed vorticty.

Fig. 12 shows snapshots of the computed magnitudes of the vorticity at four time instants within one wave period for the case of T=1.1 s in Experiment A. It can be seen that the dominant direction of the vorticity should be tangent to the outer surface of the OWC chamber, which is z direction at any point on the mirror-symmetric plane in the coordinate system used here. We chose to use the vorticity at a location on the mirror-symmetric plane and 1 cm below the lower tip of the OWC chamber skirt. This location is representative of the vorticity shed from the lower tip (see Appendix A). The $z-$ component of the vorticity vector at a given location, $\omega_z(t)$ can be written as,

$$\omega_z(t) = \frac{1}{2}\int_{-\infty}^{\infty} \Omega_z(f) e^{-2\pi f t} df \tag{30}$$

We denote the amplitude spectrum of the vorticity $\omega_z(t)$ as $\Omega(f) = |\Omega_z(f)|$.

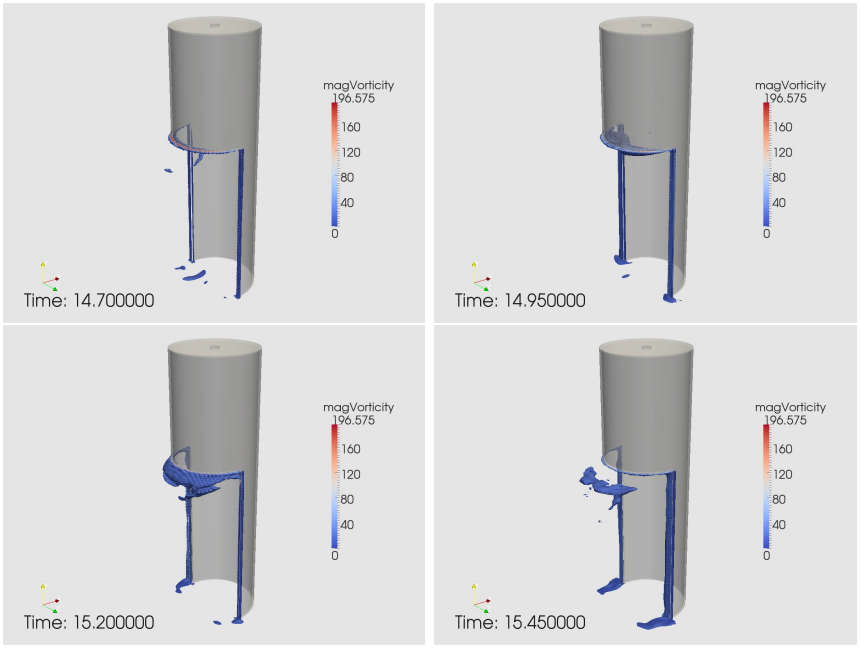

Fig. 12: Snapshots of the computed magnitudes of the vorticity at four time instants.

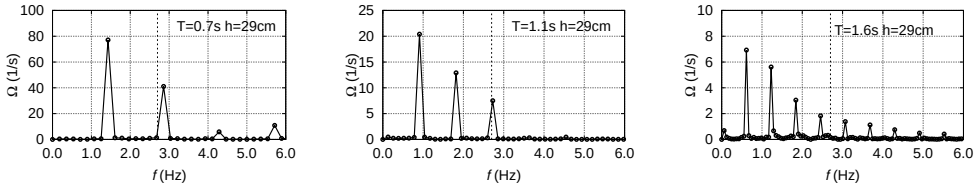

Fig. 13: Simulated amplitude spectra of the vorticity component ω_z for T= 0.7 s (left), T=1.1 s (middle) and T =1.6 s (right). The OWC chamber is fully open to the air.

Fig. 13 shows the vorticity spectra at a location 1cm below the lower skirt of the OWC chamber along the central axis, for the cases of T=0.7 s T=1.1 s, and T=1.6 s in Experiment A, but without PTO (i.e., the OWC chamber is fully open to the surrounding air). At this location, the vorticity component ω_z is tangent to the outer surface of the OWC chamber. The vorticity spectrum for T=0.7 s has four harmonics, and the vorticity spectrum for T=1.1 s has three harmonics. The vortex shedding can generate fluctuating pressure, which can generate free waves of various frequency components: for T=0.7 s the second harmonic fluctuation of the vorticity is able to excite the resonant sloshing; for T=1.1 s the third harmonic fluctuation of the vorticity is able to excite the resonant sloshing; for T=1.6 s, no harmonic fluctuation of the vorticity is close to the resonant sloshing frequency to excite the resonant sloshing. Of course, the nonlinear PTO will modify the amplitude spectrum

of the vorticity through the generation of the radiated waves. For the cases of T=0.7 s T=1.1 s, and T=1.6 s in Experiment B , but without PTO (figures are not shown here), conclusions same as those for the corresponding cases in Experiment A can be drawn.

5. Effects of sloshing motion inside the OWC chamber

Due to the lack of a good method to accurately measure the complex 3D motion of the water surface inside the OWC chamber, wave-flume experiments rely on a very limited number of wave gauges to measure the displacements of the water surface at one (Morris-Thomas et al., 2007; Xu et al., 2016; Ning et al., 2016) or two locations (He and Huang, 2014) inside the OWC chamber. The existence of the surface sloshing inside the OWC chamber causes the velocity measured at a single point to be larger than the spatial-average velocity, and thus affects the experimentally-determined capture width ratio and the measured characteristics of the nonlinear PTO (because the calculation of both needs the spatially-average velocity of the water surface inside the OWC chamber).

5.1. Effects on parameterization of the nonlinear PTO

Data fitting using Eq. (23) to both the laboratory data (Xu et al., 2016) and the simulation data has indicated that for the small-scale model as tested, the effect of inertia in $p(t)$ is very small (less than 3%) and thus negligible. Fig. 14 shows the values of the quadratic loss coefficient obtained using the velocity measured at one point ($\tilde{C}_f$) and the spatial-average velocity (C_f). Difference between $\tilde{C}_f$ and C_f can be observed. As expected, this difference is smaller for longer waves and deeper draft. The sloshing will make the velocity measured at a point larger than spatial-average velocity and thus makes $\tilde{C}_f$ smaller than C_f; this is especially true when resonant sloshing occurs. The values of $\tilde{C}_f$ are smaller at L/D=6.019 and 12.450 (i.e.,T=0.7 s and 1.1 s), the two periods at which resonant sloshing occurr. The following conclusions can be drawn from Fig. 14:

1. The quadratic loss coefficient C_f is not sensitive to wave period.
2. The values of C_f and $\tilde{C}_f$ for long waves are almost the same for both Experiment A and Experiment B.

Therefore, it is possible to use the values of $\tilde{C}_f$ obtained for long waves as the average of C_f for the tested wave periods.

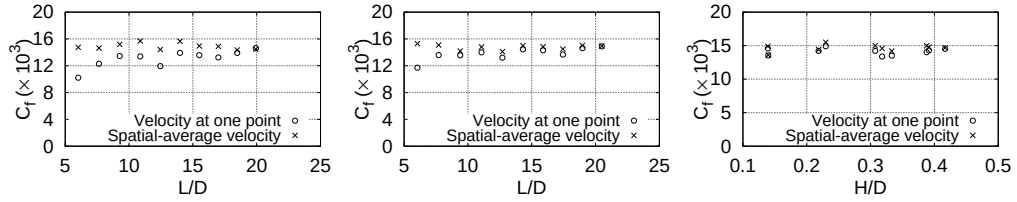

Fig. 14: Comparisons between the values of quadratic loss coefficient obtained using the velocity at location G_1 and the cross-sectional averaged velocity for Experiment A (left), Experiment B (middle) and Experiment C (right). The results presented here are based on numerical simulations.

5.2. Effects on capture width ratio

Recall that the pneumatic power extraction is calculated by

$$P_{OWC} = \frac{1}{NT}\int_{t_0}^{t_0+NT}\left[\iint_S p(t)v(x,z,t)dxdz\right]dt \tag{31}$$

which can be written as

$$\tilde{P}_{OWC} = \frac{A_0}{NT}\int_{t_0}^{t_0+NT} p(t)\bar{v}(t)dt + \frac{1}{NT}\int_{t_0}^{t_0+T}\left[\iint_S p(t)v'(x,z,t)dxdz\right]dt \tag{32}$$

Again, $\bar{v}(t)$ is the spatial average velocity and $v'(x,z,t)$ is the sloshing velocity. Note that the second term on the right hand side of Eq. (32) is zero if $v'(x,z,t)$ is known at every point on the water surface. In the experiment, $v'(x,z,t)$ is usually approximated by the value obtained at one location (x_G, z_G), i.e., $v'(x,z,t) \approx v'(x_G, z_G, t)$, which is denoted by $\tilde{v}(t)$ for simplicity hereinafter. Therefore, the approximate pneumatic power extraction is

$$\tilde{P}_{OWC} = \frac{A_0}{NT}\int_{t_0}^{t_0+NT} p(t)[\bar{v}(t)+\tilde{v}(t)]dt \tag{33}$$

The capture width ratio obtained based on one-point measurement is

$$\tilde{\lambda}/D = \tilde{P}_{OWC}/(E_I C_g D) \tag{34}$$

The error introduced by the one-point measurement method to the capture width ratio is

$$\frac{P_{OWC}-\tilde{P}_{OWC}}{E_I C_g D} = \frac{A_0}{E_I C_g DNT}\int_{t_0}^{t_0+NT} p(t)\tilde{v}(t)dt \tag{35}$$

which clearly shows that the sloshing motion will affect the capture width ratio calculated using the local velocity measured at one point inside the OWC chamber.

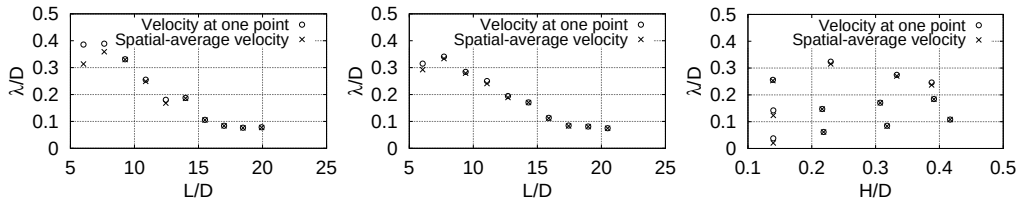

Fig. 15: Comparisons between the values of the capture length ratio obtained using the velocity at location G_2 and the cross-sectional averaged velocity for Experiment A (left), Experiment B (middle) and Experiment C (right).

Fig. 15 shows a comparison between $\tilde{\lambda}/D$ and λ/D for Experiments A, B and C. In general the values of the capture width ratios calculated using the spatial-average velocity and the local velocity measured at one point agree well except for the two shortest waves in Experiment A. For L/D=6.0186 (T=0.7 s) in Experiment A, $\tilde{\lambda}/D$ is about 20% larger than λ/D. It is interesting to note that the resonant sloshing at L/D=12.450 (T=1.1 s) does not have a significant influence on the calculated capture width ratio. In the next section, a method will be proposed to improve the accuracy of the capture width ratio calculated using one-point measurement results.

6. One method to improve the accuracy of the calculated capture width

One method to reduce the measurement error in the capture width ratio determined by using the velocity obtained from one wave gauge is to use the PTO model given by Eq. (23) and a constant quadratic loss coefficient determined for long waves. Because the inertial effect is not important for small OWC models tested in wave-flume tests (Xu et al., 2016), we can set $L_g = 0$, and then the pressure can be written as

$$p(t) = \frac{1}{2} C_f \rho_a \left|\bar{v}(t)\right| \bar{v}(t) \tag{36}$$

Using Eq. (36) in Eq. (18) gives

$$P_{OWC} = \frac{A_0}{T} \int_{t_0}^{t_0+T} \int p(t)\bar{v}(t)dt = \frac{1}{2} C_f \rho_a \frac{A_0}{T} \int_{t_0}^{t_0+T} \left|\bar{v}(t)\right|^3 dt \tag{37}$$

From Eq. (36), we have

$$\left|p(t)\right| = \frac{1}{2} C_f \rho_a \left|\bar{v}(t)\right|^2 \tag{38}$$

or

$$\left|\bar{v}(t)\right|^3 = 2\sqrt{2} \left[\frac{\left|p(t)\right|}{C_f \rho_a}\right]^{3/2} \tag{39}$$

Using Eq. (39) in Eq. (37) gives

$$P_{OWC} = \frac{\sqrt{2}A_0}{T\sqrt{C_f \rho_a}} \int_{t_0}^{t_0+T} |p(t)|^{\frac{3}{2}} dt, \tag{40}$$

Because the pressure measured in wave-flume experiment is not affected by the sloshing motion, if we can have a better estimation of C_f, Eq. (40) can be used to calculate the capture width ratio for waves that may cause large errors due to the surface sloshing inside the OWC chamber. We remark that Fleming and Macfarlane (2017a) has suggested the use of air pressure to better calculate the rate of the air flow through the orifice.

Fig. 16 shows three comparisons to support the use of Eq. (40) to calculate the capture width ratio. The left panel of Fig. 16 shows a comparison between the values of the capture width ratios calculated using the spatial average velocity and Eq. (40) with individual values of C_f; it can be seen that Eq. (40) can provide an accurate determination of the capture width ratio if an accurate estimation of C_f is available. The middle panel of Fig. 16 shows a comparison between the values of the capture width ratios calculated using Eq. (40) with individual values of C_f and a mean value of C_f obtained from the spatial-average velocity; it can be seen that it is possible to use a constant C_f to determine the capture width ratio with good accuracy. The right panel of Fig. 16 shows a comparison between the values of the capture width ratio calculated using Eq. (40) with a constant C_f (the mean C_f determined from the experimental results for long waves) and using Eq. (31) with the pressure and velocity measurements from respective numerical probes; it can be seen that using the mean $\tilde{C}_f$ from long waves can improve the estimation of the capture width ratio for short waves such as T=0.7 and 0.8 s.

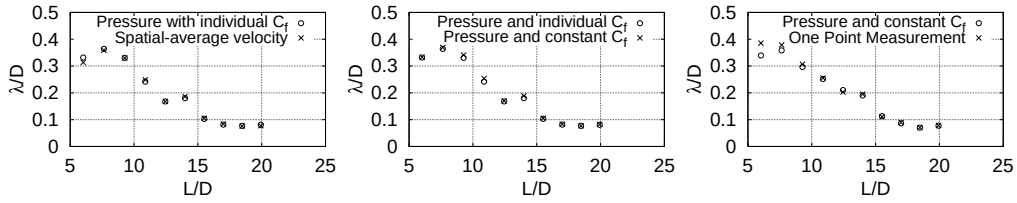

Fig. 16: Comparisons of the capture-width ratios obtained using various methods. Left panle: using pressure and spatial-average velocity and using pressure alone with individual values of C_f. Middle panel: using pressure alone with individual values of C_f and using pressure alone with the mean value of C_f determined for longer waves. Right panel: using pressure alone with the mean value of C_f determined for long waves and using pressure and the local velocity obtained at a single point.

Therefore, it is possible to use the measured pressure and a good estimation of C_f to reduce the measurement introduced to the capture width ratio by the one-point measurement method. Because the sloshing motion for longer waves is negligible, a mean value of C_f can be determined by using wave-flume experimental results for

long waves; Using this mean value of C_f and the measured pressure in Eq. (40) , we can reduce the error in the measured capture width ratio for short waves.

7. Conclusions

A CFD numerical wave flume was constructed using OpenFOAM CFD library to study a bottom-sitting 3D circular OWC-type wave energy converter. The numerical solver was based on the Reynolds-averaged Navier Stokes (RANS) equations with a modified $k-\omega$ model and a VOF method. A relaxation-zone method was used to generate regular waves and implement wave absorbing boundary condition. The numerical model was validated by comparing the numerical results with a set of existing experimental results. The validated model was used to understand the surface sloshing inside the OWC chamber. The following conclusions can be drawn from this study.

1. The CFD model was able to reproduce, with acceptable accuracy, the key measured quantities (including the free surface displacements inside and outside the OWC chamber, the pressure variation inside the OWC chamber, the quadratic loss coefficient of the PTO-simulating orifice, and the capture width ratio of the OWC device), indicating that the CFD model and the numerical setup are capable of simulating the key physical processes involved.
2. Larger measurement errors in the measured quadratic loss coefficient and capture width were found at wave periods 0.7 s and 1.1 s. The large measurement errors at these frequencies were found to be caused by spatial non-uniformity and the use of a single wave gauge inside the OWC chamber. Even though short wave length also contributed to the large measurement error for wave period 0.7 s, the measurement errors found at wave period=1.1 s were due mainly to the enhanced spatial non-uniformity. CFD simulations revealed that the resonant sloshing inside the OWC chamber was the cause for the enhanced spatial non-uniformity at these wave periods.
3. The resonant sloshing found in the physical model experiment was not excited by the fundamental waves or the higher-harmonic locked waves or the nonlinear PTO; it was excited by the vortex shedding at the sharp edge of the OWC chamber.
4. The quadratic loss coefficient was found to be weakly dependent on wave period and wave height. The capture width ratio can be calculated by using a constant quadratic loss coefficient and the measured air pressure inside the OWC pneumatic chamber.
5. The capture width ratio for shorter waves and at the periods of resonant sloshing could be determined with acceptable accuracy using the measured air pressure and the quadratic loss coefficients measured for longer waves.

Only one orifice size was examined in this study. Optimization of the pile-OWC involves optimizing the orifice size and reducing the vortex strength at the edges of the OWC chamber. This part of the work will be reported in a future study.

Acknowledgments

The material is based on work supported by the National Science Foundation under grant No. 1706938. Any opinions, findings, and conclusions or recommendations expressed in this material are those of the author(s) and do not necessarily reflect the views of the National Science Foundation. This is SOEST contribution No. **10777**.

Appendix A. Spatial variation of vorticity

As is demonstrated in Fig. 12, the vorticity along the lower edge of the OWC chamber does not have a large spatial variation. To show this, we include here plots showing the vorticity spectra at four locations in the vicinity of the lower edge of the OWC chamber skirt. The four locations are shown in Fig. Appendix A.1.

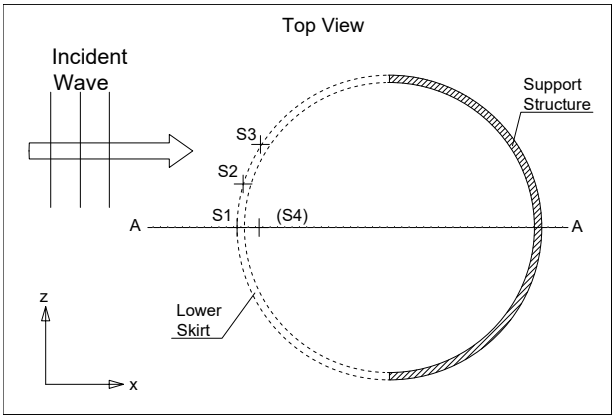

Fig. Appendix A.1: Four locations where where the vorticity spectra are analyzed. The transect A-A indicates the mirror-symmetry plane of the model. Points S1-S3 are located 1 cm below the lower tip of the OWC chamber skirt. S1 is on the A-A transect, S2 is 1.5 cm away from the A-A transect, S3 is 3 cm away from the A-A transect.The point S4 is located 1 cm below point S1.

As an example, Fig. Appendix A.2 shows the spectra of the vorticity component tangential to the outer surface of the OWC chamber at the four locations shown in Fig. Appendix A.1 for T =0.7 s. Comparing the spectra among S1, S2 and S3 reveals that there is a slightly decrease in the vorticity along the lower skirt, but the peaks close to the resonant sloshing frequency (2.72 Hz) persist. Therefore, the tangential components of the vorticity along the tip of the lower skirt do not have large variation. Comparing the spectra at S_1 and S_4 reveals the same spectrum features, even through the spectrum magnitude at the location S_4 is smaller than that at the location S_1 due to the decay of the vorticity. We conclude that the vorticity at the location S_1 is representative of the vorticity shed from the lower tip of the OWC chamber skirt.

Appendix B. Implementation of Waves2Foam

The simulations are based on Waves2Foam tutorial "waveFlume". Except for the changes to the solver itself, turbulence closure, and the computational domain,

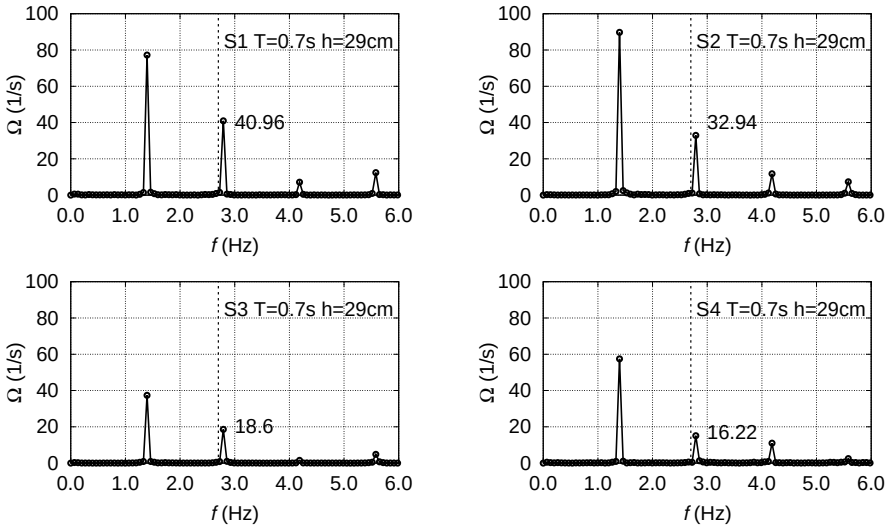

Fig. Appendix A.2: Amplitude spectra of the vorticity component ω_z for T= 0.7 s, showing results sampled at point S1, S2, S3 and S4.

there are also changes to the numerical schemes. Wherever applicable, the numerical schemes with second order accuracy and better boundedness are used for spatial and time discretizations (i.e., mixed Crank-Nicolson scheme in time, limited linear scheme in space). The boundary conditions are almost the same as those in the waveFlume tutorial, with the following exceptions:

1. For 3-dimensional computational domain, the lateral boundaries need to be changed from "empty" to "wall" (no slip boundary condition for velocity field and zero gradient for α, p, k, ω and ν_t).
2. The patch representing the surface of the OWC model generated by "snappyHexMesh" needs to be set to "wall".

The glass side walls of the wave flume and the OWC model's gloss surface of the stainless steel can be considered hydraulically smooth, so surface roughness does not need to be considered in the simulations.

For the wave generation boundary condition, two wave types were considered in the simulations: "stokesFirst" and "stokesSecond". The incident wave height specified in the wave generation file for each case (H_s) was slightly different from the value measured in the wave-flume experiment (H_t) to make sure that the wave height in the test section is close enough to the wave height measured in the experiment. Table B.2 lists the values of H_t and H_s for Cases 1a-1j,

References

Bingham, H. B., Ducasse, D., Nielsen, K., Read, R., 2015. Hydrodynamic analysis of oscillating water column wave energy devices. Journal of Ocean Engineering and

Table B.2: A summary of input wave parameters test cases 1a-1j.

T	0.7	0.8	0.9	1.0	1.1	1.2	1.3	1.4	1.5	1.6
H_t	0.037	0.038	0.039	0.038	0.039	0.036	0.037	0.038	0.038	0.038
H_s	0.038	0.037	0.037	0.036	0.039	0.037	0.036	0.036	0.036	0.036

Marine Energy 1 (4), 405–419.

Boake, C. B., Whittaker, T. J., Folley, M., Ellen, H., et al., 2002. Overview and initial operational experience of the LIMPET wave energy plant. In: The Twelfth International Offshore and Polar Engineering Conference. Vol. 1. International Society of Offshore and Polar Engineers, pp. 586–594.

Deng, Z. Z., Huang, Z. H., Law, A. W. K., 2013. Wave power extraction by an axisymmetric oscillating-water-column converter supported by a coaxial tube-sector-shaped structure. Applied Ocean Research 42, 114–123.

Deng, Z. Z., Huang, Z. H., Law, A. W. K., 2014. Wave power extraction from a bottom-mounted oscillating water column converter with a V-shaped channel. Proceedings of the Royal Society A: Mathematical, Physical and Engineering Sciences 470, 20140074.

Elhanafi, A., Fleming, A., Macfarlane, G., Leong, Z., 2016. Numerical energy balance analysis for an onshore oscillating water columnwave energy converter. Energy 116, 539–557.

Elhanafi, A., Fleming, A., Macfarlane, G., Leong, Z., 2017a. Underwater geometrical impact on the hydrodynamic performance of an offshore oscillating water column-wave energy converter. Renewable Energy 105, 209–231.

Elhanafi, A., Macfarlane, G., Fleming, A., Leong, Z., 2017b. Scaling and air compressibility effects on a three-dimensional offshore stationary OWC wave energy converter. Applied Energy 189, 1–20.

Evans, D., 1978. The Oscillating Water Column Wave-energy Device. IMA Journal of Applied Mathematics 22, 423–433.

Evans, D., 1982. Wave-power absorption by systems of oscillating surface pressure distributions. Journal of Fluid Mechanics 114, 481–499.

Evans, D., Porter, R., 1995. Hydrodynamic characteristics of an oscillating water column device. Applied Ocean Research 17 (3), 155–164.

Falcão, A. F., 2010. Wave energy utilization: A review of the technologies. Renewable and Sustainable Energy Reviews 14 (3), 899 – 918.

Falnes, J., 2007. A review of wave-energy extraction. Marine Structures 4, 185–201.

Ferziger, J. H., Peric, M., 2012. Computational methods for fluid dynamics. Springer Science & Business Media.

Fleming, A., Macfarlane, G., 2017a. In-situ orifice calibration for reversing oscillating flow and improved performance prediction for oscillating water column model test experiments. International journal of marine energy 17, 147–155.

Fleming, A. N., Macfarlane, G. J., 2017b. Experimental flow field comparison for a series of scale model oscillating water column wave energy converters. Marine Structures 52, 108–125.

Goda, Y., Nakada, H., Ohneda, H., Suzuki, M., Takahashi, S., Shikamori, M., 1991. Results of field experiment of a wave power extracting caisson breakwater. In: Proceedings of Civil Engineering in the Ocean. Vol. 7. Japan Society of Civil Engineers, pp. 143–148.

He, F., Huang, Z., 2014. Hydrodynamic performance of pile-supported OWC-type structures as breakwaters: An experimental study. Ocean Engineering 88, 618 – 626.

He, F., Huang, Z., 2017. Characteristics of orifices for modeling nonlinear power take-off in wave-flume tests of oscillating water column devices. Journal of Zhejiang University-SCIENCE A 18 (5), 329–345.

He, F., Huang, Z., Law, A. W.-K., 2013. An experimental study of a floating breakwater with asymmetric pneumatic chambers for wave energy extraction. Applied energy 106, 222–231.

Issa, R., 01 1986. Solution of the implicit discretized fluid flow equations by operator splitting. Journal of Computational Physics 62.

Iturrioz, A., Guanche, R., Lara, J. L., Vidal, C., Losada, I. J., 2015. Validation of OpenFOAM® for Oscillating Water Column three-dimensional modeling. Ocean Engineering 107, 222–236.

Jacobsen, N. G., Fuhrman, D. R., Fredsöe, J., 2012. A wave generation toolbox for the open-source CFD library: OpenFoam?? International Journal for Numerical Methods in Fluids 70 (9), 1073–1088.

Koo, W., Kim, M., 2010. Nonlinear time-domain simulation of a land-based oscillating water column. Journal of Waterway, Port, Coastal, and Ocean Engineering 136 (5), 276–285.

Liu, Z., Hyun, B. S., Hong, K. Y., et al., 2008. Application of numerical wave tank to OWC air chamber for wave energy conversion. In: The Eighteenth International Offshore and Polar Engineering Conference. International Society of Offshore and Polar Engineers, pp. 350–356.

López, I., Pereiras, B., Castro, F., Iglesias, G., 2016. Holistic performance analysis and turbine-induced damping for an OWC wave energy converter. Renewable Energy 85, 1155–1163.

Lovas, S., Mei, C. C., Liu, Y., 2010. Oscillating water column at a coastal corner for wave power extraction. Applied Ocean Research 32 (3), 267–283.

Martins-Rivas, H., Mei, C. C., 2008. Wave power extraction from an oscillating water column at the tip of a breakwater. Journal of Fluid Mechanics 626, 395–414.

Mayer, S., Madsen, P. A., 2000. Simulation of Breaking Waves in the Surf Zone using a Navier-Stokes Solver. Proceeding to Coastal Engineering Conference I, 928–941.

Medina-Lopez, E., Allsop, N., Dimakopoulos, A., Bruce, T., 2015. Conjectures on the Failure of the OWC Breakwater at Mutriku. In: Proceedings of Coastal Structures and Solutions to Coastal Disasters Joint Conference, Boston, Massachusetts. pp. 1–12.

Mei, C. C., Stiassnie, M., Yue, D. K.-P., 1989. Theory and Applications of Ocean Surface Waves: Part 1: Linear Aspects Part 2: Nonlinear Aspects. World Scientific.

Morris-Thomas, M. T., Irvin, R. J., Thiagarajan, K. P., 2007. An Investigation Into the Hydrodynamic Efficiency of an Oscillating Water Column. Journal of Offshore Mechanics and Arctic Engineering 129 (4), 273–278.

Ning, D., Shi, J., Zou, Q., Teng, B., 2015. Investigation of hydrodynamic performance of an OWC (oscillating water column) wave energy device using a fully nonlinear HOBEM (higher-order boundary element method). Energy 83, 177–188.

Ning, D., Wang, R., Zou, Q., Teng, B., 2016. An experimental investigation of hydrodynamics of a fixed OWC Wave Energy Converter. Applied Energy 168, 636 – 648.

Rapaka, E. V., Natarajan, R., Neelamani, S., 2004. Experimental investigation on the dynamic response of a moored wave energy device under regular sea waves. Ocean Engineering 31 (5-6), 725–743.

Ris, R., Holthuijsen, L., Booij, N., 1999. A third-generation wave model for coastal regions: 2. verification. Journal of Geophysical Research: Oceans 104 (C4), 7667–7681.

Rusche, H., 2003. Computational fluid dynamics of dispersed two-phase flows at high phase fractions. Ph.D. thesis, Imperial College London (University of London).

Sarmento, A. J. N. A., Falcão, A. F. O., 1985. Wave generation by an oscillating surface-pressure and its application in wave-energy extraction. Journal of Fluid Mechanics 150, 467–485.

Simonetti, I., Cappietti, L., El Safti, H., Oumeraci, H., 2015. Numerical Modelling of Fixed Oscillating Water Column Wave Energy Conversion Devices: Toward Geometry Hydraulic Optimization. In: Proceedings of the ASME 2015 34th International Conference on Ocean, Offshore and Arctic Engineering. Vol. 9. pp. 1–10.

Teixeira, P. R., Davyt, D. P., Didier, E., Ramalhais, R., 2013. Numerical simulation of an oscillating water column device using acode based on Navier-Stokes equations. Energy 61, 513–530.

Thorpe, T. W., 1999. A brief review of wave energy. Harwell Laboratory, Energy Technology Support Unit London.

Torre-Enciso, Y., Ortubia, I., de Aguileta, L. L., Marqués, J., 2009. Mutriku wave power plant: from the thinking out to the reality. In: Proceedings of the 8th European Wave and Tidal Energy Conference, Uppsala, Sweden. Vol. 710. pp. 319–329.

Versteeg, H. K., Malalasekera, W., 2007. An introduction to computational fluid dynamics: the finite volume method. Pearson Education.

Vyzikas, T., Deshoulières, S., Barton, M., Giroux, O., Greaves, D., Simmonds, D., 2017. Experimental investigation of different geometries of fixed oscillating water column devices. Renewable Energy 104, 248–258.

Wang, D., Katory, M., Li, Y., 2002. Analytical and experimental investigation on the hydrodynamic performance of onshore wave-power devices. Ocean Engineering 29 (8), 871–885.

Wang, R., Ning, D., Zhang, C., Zou, Q., Liu, Z., 2018. Nonlinear and viscous effects on the hydrodynamic performance of a fixed OWC wave energy converter. Coastal Engineering 131, 42–50.

Weller, H., Tabor, G., Jasak, H., Fureby, C., NOV-DEC 1998. A tensorial approach to computational continuum mechanics using object-oriented techniques. Computers in Physics 12 (6), 620–631.

Wilcox, D. C., 1993. Turbulence modeling for CFD. Vol. 2. DCW industries La Canada, CA.

Wilcox, D. C., 2008. Formulation of the kw turbulence model revisited. AIAA Journal 46 (11), 2823–2838.

Xu, C., Huang, Z., Deng, Z., apr 2016. Experimental and theoretical study of a cylindrical oscillating water column device with a quadratic power take-off model. Applied Ocean Research 57, 19–29.

Zhang, Y., Zou, Q., Greaves, D., 2012. Air-water two-phase flow modelling of hydrodynamic performance of an oscillating water column device. Renewable Energy 41, 159–170.